Simulation of Earth Observation Data Utilizing a Virtual Satellite Camera

NINO LENZ[1] & MICHAEL GREZA[1]

Abstract: Image chain simulation is an essential tool for the design of Earth observation satellites. In this work, a simulator for the images produced by an upcoming low Earth orbit remote sensing nanosatellite constellation by the Technical University of Munich, Center for Telematics Würzburg and the Bavarian Surveying and Mapping Authority is developed. Projection and sampling models adjusted for this application are presented. The system's modulation transfer function is estimated according to analytical models for atmosphere, sensor, and optical system effects. Images are simulated based on digital orthophotos and the desired satellite orbit.

Disturbances of the ideal orbits are introduced, and their impact on the appearance of the produced images is explored. A comparison with other nanosatellite remote sensing missions is used to estimate expected inaccuracies resulting from attitude deviations. The localization of real and fictional ground control points is employed to estimate positional inaccuracies in the simulated images caused by a lack of information about terrain shape and elevation.

1 Introduction

Historically, satellite missions have been characterized by long development cycles and high costs, in part due to the large size of satellites. However, technical advances have made much smaller designs feasible in the last few decades. Standardized dimensions allow the deployment of many nanosatellites at once by hitching a ride on a larger launch vehicle as a secondary payload. Economies of scale and reduced launch costs have dramatically lowered the entry barrier to satellite missions (CRUSAN & GALICA 2019).

Unlike many other engineering applications, for satellites, adjustments to the system design can - if at all - only be made in software after deployment, and serviceability is essentially zero. Where functionality cannot be tested directly, extensive simulation of the system is therefore required to assess the expected behavior. A simulation of the imaging subsystem can confirm that goals and requirements of the mission will be met or indicate if design changes need to be made.

In this work, a simulator for the images produced by a low Earth orbit remote sensing nanosatellite with a ground sampling distance (GSD) of roughly 4 m is presented. A priority is the precise rendering of the planned satellite orbit and the resulting ground coverage. In addition, the appearance of the produced images is adjusted to account for properties of a line scan camera, atmosphere, and satellite movement. The focus will be on questions of spatial resolution, rather than radiometric qualities. Several simulations are run to assess the expected image quality, and to investigate the influence of different parameters on the simulation results.

[1] Technische Universität München, Photogrammetrie und Fernerkundung, Arcisstr. 21, 80333 München, E-Mail: [nino.lenz, michael.greza]@tum.de

 DOI: 10.24407/KXP:1841067350

The generation of artificial satellite imagery is an experimental part of a simulation toolkit in an ongoing research collaboration for the development of a low Earth orbit remote sensing nanosatellite constellation between the Technical University of Munich, the Center for Telematics Würzburg and the Bavarian Surveying and Mapping Authority.

2 Related Work

Previous work on the simulation of satellite-based Earth-observation data tends to focus more on the resulting image quality with regards to MTF, resolution, noise, or radiometric characteristics, rather than the precise simulation of viewing geometry and position based on prescribed orbits. In accordance with this, several authors chose to carry out most calculations in the frequency domain (e.g. ALICI et al. 2019; COTA et al. 2008; WAHBALLAH et al. 2021). However, since certain properties of imaging systems are represented in the spatial domain more easily or precisely, some research has been done in this regard as well (BÖRNER et al. 2001; CHEN et al. 2009). Regardless of spatial or frequency domain, the simulations tend to follow a similar scheme.
The input dataset should provide significantly higher spatial and/or spectral resolution than the simulated imaging system and high SNR to be suitable for use as "ground truth" data, on which the simulation is based. The use of approximate inferences about the acquisition conditions, in conjunction with other software tools such as MODTRAN, allows for the conversion of aerial imagery data to values of bottom-of-atmosphere radiance.
In subsequent steps, effects representing illumination conditions and interactions with the atmosphere, the camera's optical system, movement of the satellite, and properties of the camera sensor are applied. The modified input data is downsampled and quantized to receive the output image.

3 Methods

3.1 Input Data

The input data for the simulation consists of the nominal satellite orbits, containing satellite position and attitude, a digital orthophoto (DOP) of the region to be recorded, and a list of ground control points (GCPs) whose position in the output image is to be determined. The orbits are provided by Astronomical and Physical Geodesy of TU Munich while the DOPs and GCPs are provided by the Bavarian Surveying and Mapping Authority.
In the context of the simulator, the DOP is assumed as the ground truth, i.e., as an image obtained by an ideal camera, without any losses in resolution or other effects degrading the image quality. In reality, the DOP was recorded using real, imperfect cameras. However, since the expected resolution of the simulated images (GSD ~4 m) is much lower than that of the DOP (0.2 – 0.4 m), these imperfections are regarded to have negligible impact on the simulation results.

3.2 Simulator Design Procedure

To model the degradation of the data due to the simulated imaging process, a system model is created, and supplied with mission-specific camera and orbit parameters. Steps in the image chain

are simulated individually, and finally compiled into an overall modulation transfer function (MTF). Where detailed mission-specific information is not yet available, typical values are substituted from literature.
It should be noted that only narrow-bandwidth spectra will be considered here, such that all wavelength-dependent quantities can be assumed as constant within a single band. For sensors with multiple narrow bands, the wavelength-dependent effects should therefore be applied to each band separately. While the DOP used in this paper provides only RGB bands, the simulator is capable of generating multispectral images as well, given suitable input data.
Further, a sophisticated attempt to determine radiometric properties, as mentioned in section 2, is omitted due to its reliance on external software and since questions of spectral resolution are not the focus of this work. In absence of more information about the original acquisition system, the DOP data is instead assumed to express bottom-of-atmosphere radiance values of unknown units. As such, a high degree of radiometric accuracy cannot be expected from the simulated images.

3.3 Experiments

Once suitable parameters for the simulation have been determined, the image swaths are simulated according to the provided nominal satellite orbits. The system MTF curve and its components are presented.
In addition, the effects of deviations from nominal attitude are investigated. For this purpose, sinusoidal oscillations in the satellite's pitch and roll angles are introduced to simulate gyroscopic motion. The magnitude and frequency of the deviations are varied in order to estimate their effects on image quality. Allowable tolerances and different effects on the appearance of produced images are explored.
The impact of elevation differences on positional accuracy is investigated. To this end, the positions of GCPs are specified once at their actual elevations, and once assumed to all lie in the same horizontal plane. The differences in their positions in the simulated images are determined to assess the possible benefits of introducing a digital surface model (DSM). In a second step, fictional GCPs are introduced to better quantify the errors caused by the absence of a DSM. Determining parameters for the magnitude of the errors are identified and a model for rough error estimation presented.

4 Simulator Design

4.1 Simulation Workflow

To satisfy the requirement of high positional fidelity, the primary part of the image acquisition is simulated in the spatial domain. According to the projection model discussed below, the image is assembled line-by-line based on the given satellite positions and attitudes. In a second step, this "raw" simulated image is degraded further by applying the MTF and finally adding noise.

4.2 Projection Model

The line sensor is continuously exposed to the incident radiation, and the accumulated charge read out in regular intervals. These aspects are taken into account by the following model.

The terrain, or rather the input DOP, is assumed to be perfectly flat and lie in a horizontal plane at a specified elevation. This elevation should therefore be chosen to represent the region of interest as well as possible.
The line sensor is modelled as a one-dimensional line, which is made up of segments representing an individual pixel each. The pixels' corner points are then projected onto the DOP plane. This projection is performed once from the exterior orientation at the beginning and again at the end of each sampling period. By constructing quadrilaterals from the four corner coordinates obtained for each pixel in this way, the continuous area covered by the satellite swath is obtained, without the possibility of gaps occurring between subsequent exposures. Figure 1 illustrates this projection model.

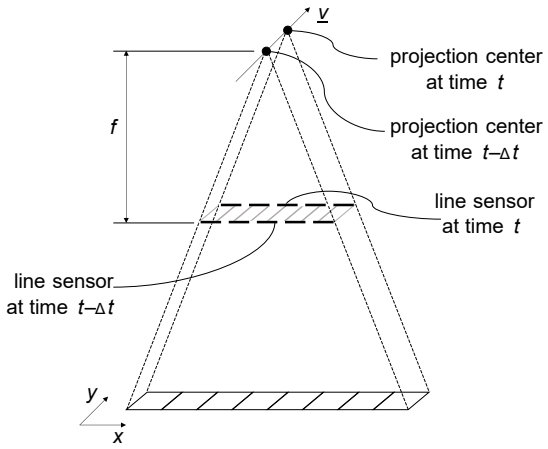

Fig. 1: Projection model

Once the projected quadrilateral corresponding to a pixel has been obtained in this way, the given GCPs are checked for intersection with the projected area using a ray tracing algorithm to ensure correct localization independent of a GCP's elevation. Finally, the value of the pixel in the raw simulated image is computed as the mean value of all DOP pixels contained within the quadrilateral.
The resulting projection is thus a mix of the central and parallel projection models: While it realizes a central perspective in the across-track direction, the along-track sweep is modelled in parallel perspective.

4.3 Modulation Transfer Function

The individual steps in the image chain are simulated by choosing appropriate analytical MTF models, and parameters are adjusted based on the camera datasheet, orbit data, and typical values found in literature. The MTF is expressed in terms of spatial frequencies in the focal plane, with k_x denoting frequencies in the across-swath direction, and k_y denoting frequencies along the flight direction. The following definitions are useful for discussion of some of the imaging steps: the radial spatial frequency k_r, diffraction-limited cutoff frequency k_{co}, and normalized spatial frequency k_n, as given in eq. 1.

$$k_r = \sqrt{k_x^2 + k_y^2}, \qquad k_{co} = \frac{D}{\lambda f}, \qquad k_n = \frac{k_r}{k_{co}} \tag{1}$$

with primary aperture diameter D, incoming radiation wavelength λ, and focal length f.
Turbulence in the atmosphere degrades image quality according to eq. 2 to 3 (ALICI et al. 2019; HOLST 2000), while aerosols cause scattering and absorption according to eq. 4 (ALICI et al. 2019; HOLST 2000; SADOT & KOPEIKA 1994).

$$MTF_{turbulence} = \exp\left(-3.44\ \left(\frac{\lambda\, f\, k_r}{r_0}\right)^{\frac{5}{3}}\left[1-\alpha\left(\frac{\lambda\, f\, k_r}{D}\right)^{\frac{1}{3}}\right]\right) \tag{2}$$

$$r_0 = 0.185\,\lambda^{\frac{6}{5}}\left[\int_0^H \left(\frac{h}{H}\right)^{\frac{5}{3}} C_n^2(h)\,dh\right]^{-\frac{3}{5}}, \qquad \mathrm{C_n^2(h)} = 4.16\times 10^{-13} m^{\frac{2}{3}}\ h^{\frac{-4}{3}} \tag{3}$$

where r_0 is the atmospheric coherence diameter, and H the satellite's altitude above ground.

$$MTF_{aerosol} = \begin{cases} \exp\left(-A_a\, l_{opt} - S_a\, l_{opt}\,(\frac{k_r}{k_{aco}})^2\right), & \frac{k_r}{k_{aco}} \le 1 \\ \exp\left(-A_a\, l_{opt} - S_a\, l_{opt}\right), & \frac{k_r}{k_{aco}} > 1 \end{cases} \tag{4}$$

with atmospheric absorption and scattering coefficients A_a and S_a, optical path length l_{opt}, and aerosol cutoff frequency k_{aco}.
Diffraction around its aperture limits the spatial frequencies resolvable by the camera. A suitable model for the simulated Cassegrain optical system is used to represent the decreasing MTF behavior (COTA et al. 2008; O'NEILL 1956), as shown in eq. 5 through 9.

$$MTF_{diffraction} = \frac{2}{\pi}\,\frac{A+B+C}{1-\epsilon^2} \tag{5}$$

$$A = \arccos(k_n) - k_n\sqrt{1-k_n^2} \tag{6}$$

$$B = \begin{cases} \epsilon^2\left[\arccos\left(\frac{k_n}{\epsilon}\right) - \frac{k_n}{\epsilon}\sqrt{1-\left(\frac{k_n}{\epsilon}\right)^2}\right], & k_n \le \epsilon \\ 0, & k_n > \epsilon \end{cases} \tag{7}$$

$$C = \begin{cases} -\pi\epsilon^2, & k_n \le \frac{1-\epsilon}{2} \\ -\pi\epsilon^2 + \epsilon\sin(\phi) + \frac{\phi}{2}(1+\epsilon^2) - (1-\epsilon^2)\arctan\left(\frac{1+\epsilon}{1-\epsilon}\tan\left(\frac{\phi}{2}\right)\right), & \frac{1-\epsilon}{2} < k_n \le \frac{1+\epsilon}{2} \\ 0, & k_n > \frac{1+\epsilon}{2} \end{cases} \tag{8}$$

$$\phi = \arccos\left(\frac{1+\epsilon^2-4k_n^2}{2\epsilon}\right), \qquad \epsilon = \frac{D_{obscuration}}{D} \tag{9}$$

with D the primary aperture diameter, and $D_{obscuration}$ the diameter of the circular obscuration mirror.
In addition, a variety of aberrations in the optical system can affect image quality. Since their exact nature is generally not known in the early stages of the design process, their influence can be approximated by the expected wavefront error. Using a model based on its root-mean-square W_{RMS} as in eq. 10 (ALICI et al. 2019; HOLST 2000), the wavefront error is adjusted to match MTF values specified by the optical system manufacturer.

$$MTF_{WFE} = 1 - \left(\frac{W_{RMS}}{0.18}\right)^2\left[1 - 4\,\left(\mathrm{k_n} - \frac{1}{2}\right)^2\right] \tag{10}$$

The accumulation of photoelectrons within the physical dimensions of a single detector pixel means that no structures smaller than these dimensions can be recovered. In other words, each

individual pixel presents a square aperture with side length w_{px}, over which the incoming signal is averaged (ALICI et al. 2019; COTA et al. 2008; WAHBALLAH et al. 2021). While in x direction this effect is already covered by the projection model, it must be accounted for by an additional term in the model MTF for the y direction as shown in eq. 11.

$$MTF_{aperture} = \operatorname{sinc}(k_y\, w_{px}) \tag{11}$$

Note that the extent of a pixel's projection on the terrain in y direction, as shown in Figure 1, does not represent the physical dimension w_{px} of the corresponding detector element. Rather, it is caused by the relative movement between the sensor and the imaged object during the exposure. The resulting unavoidable smear in flight direction is therefore also accounted for by the projection model.

However, additional smear components may arise from imperfections in the time-delay and integration (TDI) sensor setup and across-scan velocity components: A mismatch Δv_y between the time between sensor readouts and the velocity of the projected image in the focal plane degrades the image in scan direction. If the direction of flight and charge transfer direction are not perfectly parallel but form an angle θ, further degradation in across-scan direction occurs. These aspects are simulated as shown in eq. 12 to 13 (WAHBALLAH et al. 2021).

$$\Delta v_y = \frac{p_y}{t_{int}} - v_y\, \frac{f}{H} \tag{12}$$

$$MTF_{TDI} = \frac{\sin(\pi\, N_{TDI}\, w_{px}\, \tan(\theta)\, k_x)}{N_{TDI}\, \sin(\pi\, w_{px}\, \tan(\theta)\, k_x)}\, \frac{\sin(\pi\, N_{TDI}\, |\Delta v_y|\, t_{int}\, k_y)}{N_{TDI}\, \sin(\pi\, |\Delta v_y|\, t_{int}\, k_y)} \tag{13}$$

with the pitch between TDI stages p_y, the number of TDI stages N_{TDI}, and integration time t_{int}, the duration over which charge is accumulated in the sensor before readout.

Due to random movement of the electrons generated in the detector, the image is blurred further as electrons may eventually arrive in a neighboring pixel well, an effect known as charge diffusion. Different models for a corresponding MTF are available (e.g. COTA et al. 2008; DJITE et al. 2012; SHCHERBACK & YADID-PECHT 2004). In this work, the model presented in eq. 14 will be used (ALICI et al. 2019; FIETE 2010; WAHBALLAH et al. 2021)

$$MTF_{diffusion} = \left(1 - \frac{\exp(-\alpha_{abs}\, l_{dep})}{1+\alpha_{abs}\, l_K}\right)\left(1 - \frac{\exp(-\alpha_{abs}\, l_{dep})}{1+\alpha_{abs}\, l_{diff}}\right)^{-1}, \quad l_K = \frac{l_{diff}}{\sqrt{1+(2\pi\, l_{diff}\, k_r)^2}} \tag{14}$$

with absorption coefficient α_{abs}, diffusion length l_{diff}, and depletion width l_{dep}.

In addition to these effects, high-frequency random motion of the satellite system, so-called jitter, affects image quality. The displacements are modelled by a normal distribution with variance σ^2_{jitter}. The corresponding MTF is therefore a Gaussian given by eq. 15 (ALICI et al. 2019; WAHBALLAH et al. 2021).

$$MTF_{jitter} = \exp\left(-2\pi^2\, \sigma^2_{jitter}\, k_r^2\right) \tag{15}$$

It is important to note that the MTF obtained through composition of the individual steps mentioned here is not equivalent to the overall system MTF, as the steps modelled in the spatial domain – such as downsampling to the simulated image size, or linear smear in flight direction – do not explicitly appear in it.

4.4 Noise

Various sources of noise influence the output image. Photon shot noise and dark current noise are Poisson-distributed, while readout noise and noise generated by electronic circuitry are normally distributed. To simulate the different sources of noise present in the imaging system, additive white Gaussian noise is added to each output pixel and each band independently. The Poisson-distributed noise components are also approximated as normally distributed (BÖRNER et al. 2001; COTA et al. 2008).

The noise standard deviations are adjusted to match signal-to-noise ratios (SNRs) specified by the camera manufacturer for each recorded band. The Gaussian noise is added to the simulated image after application of the MTF as the last step of the simulation process.

5 Results & Discussion

Exemplary MTF curves are shown in Figure 2. The influence of the averaging due to $MTF_{aperture}$, which is only performed in the frequency domain in y direction, and instead modelled in the spatial domain in x direction, can clearly be seen. For the production of output images, the MTF was calculated for each band individually based on its central wavelength, and on a grid spanning x and y dimensions. Noise levels are given in Table 1. Simulated imagery as well as real satellite data acquired by a comparable system (PLANET 2022) are shown in Figure 3.

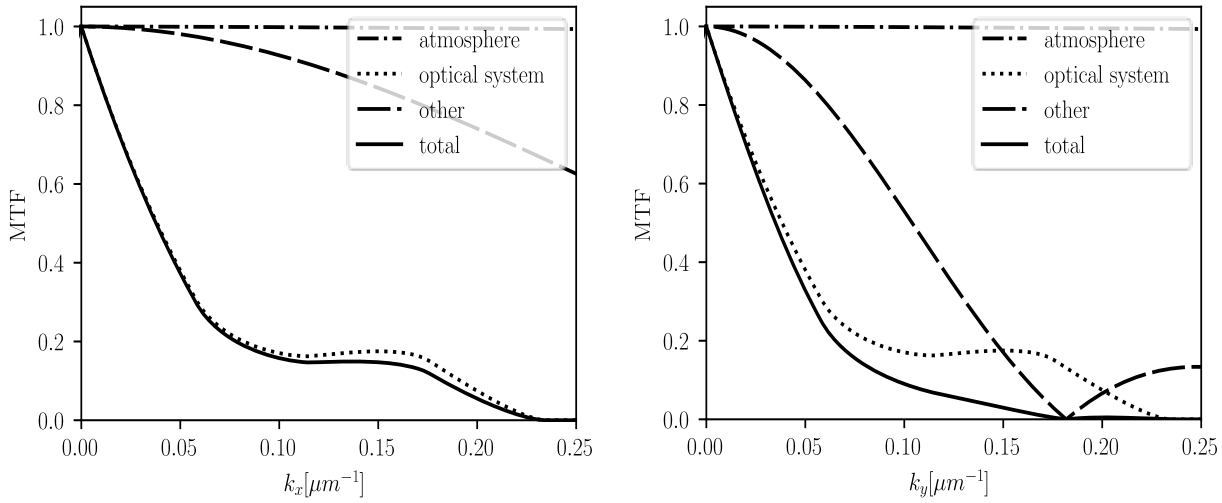

Fig. 2: MTF across (left) and in (right) flight direction

Tab. 1: SNRs and corresponding noise levels

Band	Specified SNR	Mean band value	Noise std. deviation
red	100	102.26	1.02
green	110	110.58	1.01
blue	120	101.21	0.84

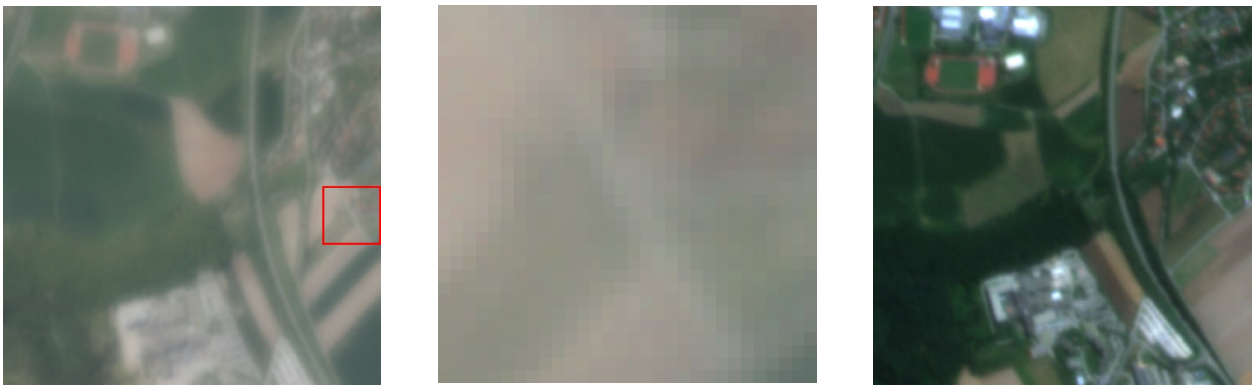

(a) Simulation, near Ansbach. (b) Simulation, zoomed in. (c) Real satellite data.

Fig. 3: (a) and (b) show sections of simulated images and (c) actual Planet satellite data to compare

5.1 Simulation of Oscillations

While small vibrations at frequencies above the line rate are modelled as jitter, slower deviations from nominal flight conditions may be simulated by applying additional translations and rotations to the orbit data. Sinusoidal oscillations of pitch and roll angles are used to simulate a gyroscopic movement or precession of the satellite. Frequency and amplitude of the oscillations are varied along the satellite's flight to investigate their effects.

Oscillations with peak-to-peak amplitudes <0.0005° are near imperceptible even in a direct comparison of the simulated images with and without disturbances. Above a certain frequency, the shape of the oscillations becomes less and less pronounced in the simulated images. Instead, the disturbances simply cause additional blurring of the image. For frequencies higher than half of the line rate, aliasing occurs according to the Nyquist theorem. These oscillations should therefore not be modelled as disturbances of the satellite attitude, but rather by taking them into account as jitter.

While in the early stages of satellite design the capabilities of the attitude control system cannot be definitively stated yet, a look at other nanosatellite missions may give an idea of the expected accuracy both in terms of tracking error and compensation of unwanted angular velocities. Using reaction wheels, the rotations can be reduced to between 3.0×10^{-3} and 0.5×10^{-3} rad/s (Li et al. 2013a), and tracking errors of 0.0010° to 0.0012° can be achieved (Li et al. 2013b; Oland & Schlanbusch 2009).

Assuming a similar accuracy for the simulated mission, a positional error of the field of view on the ground surface of a few pixels, or in the order of around 10 m, must be expected. The relatively low angular velocities, however, suggest that a significant degradation of image resolution or visible distortions of the geometry of pictured objects could be avoided. Due to the speculative nature of these considerations, however, the simulations should be repeated once better estimates of the actual attitude control capabilities are available.

5.2 Localization of Ground Control Points

Several GCPs on and below a ridge near the Zugspitze summit were fed into the program to investigate the effect the introduction of a DSM might have on the positional accuracy of the simulation. Each point was given once with its actual elevation (between 2300 m and 2962 m),

and once assumed to lie in the DOP plane (at 970 m). The resulting positions of exemplary GCPs are displayed in Figure 4a.
To better visualize the contributions to this positioning error, virtual GCPs are generated across the sensor's field of view and at varying elevations. The resulting distribution of the positioning errors Δc in pixels depending on a point's vertical offset from the DOP plane ΔZ and its position along the sensor is shown in Figure 4b.
Fitting a bilinear surface to this distribution yields an expected positioning error of 1 m for every 52.30 m of vertical offset at the sensor's edges for the given mission parameters. The bilinear model assumes a perfect nadir view, such that no error can occur in the center of the line sensor. Despite this limitation, it is a useful tool for a rough error estimation under normal flight conditions. These results demonstrate the potential gains in positional accuracy by introduction of a DSM.

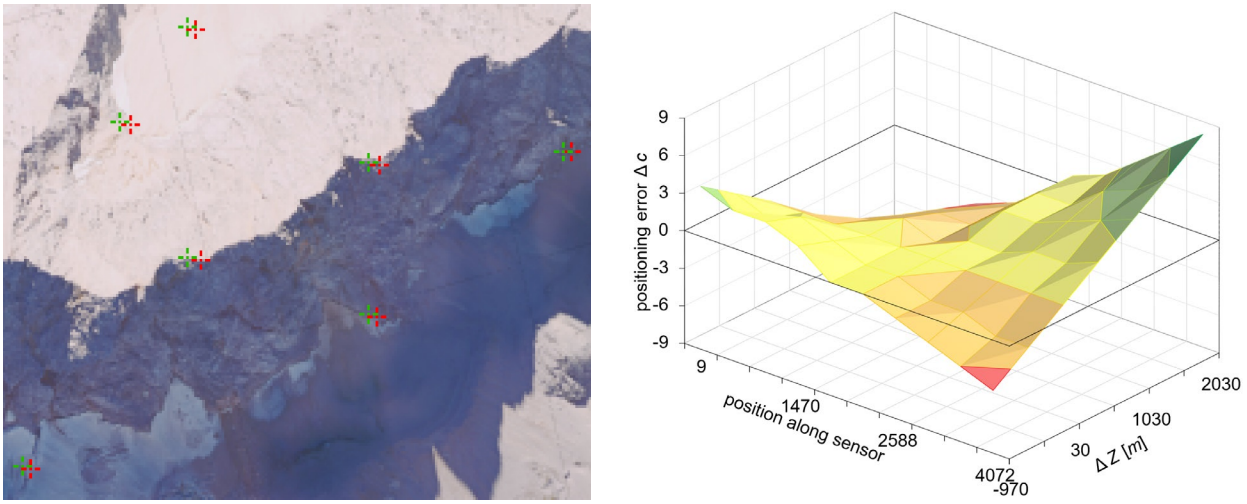

(a) Positions of GCPs near Zugspitze summit. (b) Positioning error distribution.

Fig. 4: (a) Positions of GCPs with correct elevation (green) and GCPs assumed to lie in the DOP plane (red) in a simulated image, and (b) positioning error distribution for fictional GCPs

5.3 Radiometric Properties

As discussed before, the radiometric scaling of the input image data is not known. If the prediction of radiometric quantities such as at-sensor radiance is desired, a different set of input data or more details about the original data acquisition are needed. It must be possible to establish a mapping from the original data to either surface reflectance or directly to bottom-of-atmosphere radiance to simulate images with some degree of radiometric accuracy.
Additionally, detailed knowledge of the simulated sensor characteristics, such as the magnitude of the individual components of total sensor noise, or possible non-linearity of the detector response would allow an even more exact simulation.
If the intensity of the output image can be quantified in units of radiance, it is also possible to predict the overall level of noise more accurately. Assuming photon shot noise is the dominating source of noise, the SNR is proportional to the square root of the number of generated

photoelectrons. This relation would allow to scale the noise variance according to the actual at-sensor radiance, instead of assuming a constant SNR for each band.
Without having a dataset as specified above, a quantified comparison between our simulated images and Planet images is not meaningful. Further, the Planet data is preprocessed and not raw satellite imagery. When evaluating the results via qualitative visual inspection our results, as shown in Figure 3, appear foggier with less contrast. On a geometric basis, the images are more similar.

6 Conclusion & Outlook

Our work proposes a simulator design adjusted specifically to line scanner imagery acquired by low Earth orbit satellites. Two main areas with potential for future improvements to the simulator have been identified: First, for spectral properties to be represented with any degree of accuracy, input data which allows for the inference of radiometric quantities must be used. Second, the positional accuracy of simulated images could be improved by the introduction of a DSM.
To fully assess the quality of the simulated data, the benefits of post-processing techniques such as MTF compensation should be considered. The MTF model established here may be beneficial to these investigations. Once the satellites are operational, a comparison of the resulting images with those generated by the simulator could allow for an assessment of the methods proposed here and expose further areas for improvement.

7 Bibliography

ALICI, K., OKTEM, F., KARCI, O., YILMAZ, A. & SELIMOGLU, O., 2019: Image chain simulation for earth observation satellites. IEEE Journal of Selected Topics in Applied Earth Observations and Remote Sensing, **12**(10).

BÖRNER, A., WIEST, L., KELLER, P., REULKE, R., RICHTER, R., SCHAEPMANN, M. & SCHLÄPFER, D., 2001: SENSOR: a tool for the simulation of hyperspectral remote sensing systems. ISPRS Journal of Photogrammetry and Remote Sensing, **55**(5-6), 299-312.

COTA, S., BELL, J., BOUCHER, R., DUTTON, T., FLORIO, C., FRANZ, G., GRYCEWICZ, T., KALMAN, L., KELLER, R., LOMHEIM, T., PAULSON, D. & WILLKINSON, T., 2008: PICASSO: An End-to-End Image Simulation Tool for Space and Airborne Imaging Systems. Remote Sensing System Engineering, Ardanuy, P. & Puschell, J. (Hrsg.), SPIE, Bellingham.

CHEN, X., LI, T., XUE, B., ZHANG, X., CHEN, G. & NI, G., 2009: Satellite high resolution imaging simulation in space field. International Symposium on Photoelectronic Detection and Imaging 2009: Advances in Imaging Detectors and Applications, Zhang, K., Wang, X., Zhang, G. & Ai, K. (Hrsg.), SPIE, Bellingham, 162-171.

CRUSAN, J. & GALICA, C., 2019: NASA's CubeSat Launch Initiative: Enabling Broad Access to Space. Acta Astronautica, **157**, 51-60.

DJITE, I., ESTRIBEAU, M., MAGNAN, P., ROLLAND, G., PETIT, S. & SAINT-PE, O., 2012: Theoretical models of modulation transfer function, quantum efficiency, and crosstalk for CCD and CMOS image sensors. IEEE Transactions on Electron Devices, **59**(3), 729-737.

FIETE, R., 2010: Modeling the imaging chain of digital cameras. Tutorial texts in optical engineering, **92**, SPIE, Bellingham.

HOLST, G., 2000: Electro-optical Imaging System Performance. 2nd edition. SPIE, Bellingham.

LI, J., POST, M. & LEE, R., 2013a: Real-time Nonlinear Attitude Control System for Nanosatellite Applications. Journal of Guidance, Control, and Dynamics, **36**(6), 1661-1671.

LI, J., POST, M., WRIGHT, T. & LEE, R., 2013b: Design of Attitude Control Systems for CubeSat-Class Nanosatellite. Journal of Control Science and Engineering, **2013**(5).

OLAND, E. & SCHLANBUSCH, R., 2009: Reaction Wheel Design for CubeSats. 4th International Conference on Recent Advances in Space Technologies, Kurnaz, S., Ince, F., Onbasioglu, S. & Basturk, S. (Hrsg.), 778-783.

O'NEILL, E., 1956: Transfer Function for an Annular Aperture. Journal of the Optical Society of America, **46**(4), 285-288.

PLANET, 2022: Planet Application Program Interface: In Space for Life on Earth. https://api.planet.com, letzter Zugriff 10.09.2022.

SADOT, D. & KOPEIKA, N., 1994: Effects of absorption on image quality through a particulate medium. Applied Optics, **33**(30), 7107-7111.

SHCHERBACK, I. & YADID-PECHT, O., 2004: CMOS APS MTF Modeling. CMOS Imagers: From Phototransduction to Image Processing, Yadid-Pecht, O. & Etienne-Cummings, R. (Hrsg.), Springer, Dordrecht, 53-74.

WAHBALLAH, W., LANEVE, G., EL-TOHAMY, F. & BAZAN, T., 2021: Modeling and Simulation of a Remote Sensing Satellite Camera. Sensors, Systems, and Next-Generation Satellites, **25**.